Applied Catalysis B: Environmental 256 (2019) 117844

Contents lists available at ScienceDirect

Applied Catalysis B: Environmental

journal homepage: www.elsevier.com/locate/apcatb

Origin of electronic structure dependent activity of spinel $ZnNi_xCo_{2-x}O_4$ oxides for complete methane oxidation

Ting Wang[a,b,c], Jieyu Wang[a], Yuanmiao Sun[b], Yan Duan[b,d], Shengnan Sun[b,d], Xiao Hu[b,c], Shibo Xi[e], Yonghua Du[e], Chuan Wang[a,**], Zhichuan J. Xu[b,d,*]

[a] Institute of Advanced Synthesis, School of Chemistry and Molecular Engineering, Jiangsu National Synergetic Innovation Center for Advanced Materials, Nanjing Tech University, 30 Puzhu South Road, Nanjing 211800, PR China
[b] School of Materials Science and Engineering, Nanyang Technological University, 50 Nanyang Avenue, 639798, Singapore
[c] Nanyang Environment and Water Research Institute (NEWRI), Interdisciplinary Graduate School (IGS), Nanyang Technological University, 1 Cleantech Loop, CleanTech One, 637141, Singapore
[d] Solar Fuels Laboratory, Nanyang Technological University, 50 Nanyang Avenue, 639798, Singapore
[e] Institute of Chemical and Engineering Sciences A*STAR, 1 Pesek Road, 627833, Singapore

ARTICLE INFO

Keywords:
Methane oxidation
Spinel oxide
Electronic structure
Dissociative adsorbed oxygen
Lattice oxygen

ABSTRACT

Exploring active and low-cost spinel catalysts for complete methane oxidation is essential for the development of efficient air purification technologies. Herein, a series of spinel oxides $ZnNi_xCo_{2-x}O_4$ (x = 0–0.8) were synthesized to investigate the origin of their electronic structure dependent activities and mechanisms for methane oxidation. The interplay between O *p*-band center and M_{oct} *d*-band center was found to be responsible for the methane oxidation activity. Ni-poor $ZnNi_xCo_{2-x}O_4$ spinels with the M_{oct} *d*-band center positioned higher relative to the O *p*-band center, exhibited greater metal character, indicative of a dissociative adsorbed oxygen featured suprafacial Eley-Rideal (E-R) model. In contrast, Ni-rich $ZnNi_xCo_{2-x}O_4$ with the O *p*-band center in a higher position relative to the M_{oct} *d*-band center, displayed greater oxygen character, predominated by the intrafacial Mars-van-Krevelen (Mv-K) mechanism featuring the involvement of lattice oxygen. These findings may provide steps towards the rational design of better spinel oxides for catalytic oxidation reactions.

1. Introduction

Methane, as the major constituent of natural gas, possesses a greenhouse effect that is much more prominent than CO_2 [1–3]. With the widely application of natural gas in auto-vehicles, power plants and other industries, the abatement of methane (CH_4) atmospheric emission is of paramount importance to meet the increasingly stringent environment regulations [2,4,5]. Currently, the most efficient and simple strategy to reduce the detrimental environmental effect of methane is the catalytic combustion, through which methane is completely oxidized into carbon dioxide and water [2,6]. To date, the most intensively studied catalysts are the noble metals, especially the Pd and Pt, which are found to be the most active for the catalytic combustion [7,8]. However, precious metals impose various constraints, including high cost, scarcity and strict operating temperatures (they deteriorate easily by sintering at high temperatures) [6,7,9].

Transition metal oxides such as spinels [1,4,10–12], perovskites [8,13–15] and some mixed oxides [2,8,16,17] are considered as potential alternatives due to their distinctly lower prices and promising catalytic activities. Among them, the cobalt-based spinel oxides are found to be one of the most intriguing catalysts which exhibit high catalytic activities [1,4,10–12]. For instance, different-shaped Co_3O_4 nanocrystals [18] including sheets, belts, and cubes all display a T_{90} (the temperature where 90% of methane is converted) lower than 673 K, which is comparable or even lower than supported Pd catalysts under similar reaction conditions [7]. Comparable catalytic performance has also been reported on a series of manganese cobalt spinel oxides, with the best one achieving 90% conversion of methane at 593 K [1]. The explanations for the high catalytic activity of cobalt spinel oxides vary dramatically. For instance, some considered the relatively low bonding energy of Co—O bond along with the multifold surface lattice O as the main responsible reason [9], while some others

* Corresponding author at: School of Materials Science and Engineering, Nanyang Technological University, 50 Nanyang Avenue, 639798, Singapore.
** Corresponding author at: Institute of Advanced Synthesis, School of Chemistry and Molecular Engineering, Jiangsu National Synergetic Innovation Center for Advanced Materials, Nanjing Tech University, 30 Puzhu South Road, Nanjing 211800, PR China.
E-mail addresses: ias_cwang@njtech.edu.cn (C. Wang), xuzc@ntu.edu.sg (Z.J. Xu).

https://doi.org/10.1016/j.apcatb.2019.117844
Received 2 April 2019; Received in revised form 4 June 2019; Accepted 7 June 2019

simply attributed the high activity to the increased amount of octahedrally coordinated cobalt cations [1]. Therefore, further investigation is needed for a more comprehensive understanding of the origin of oxidation activity. Nickel, another active transition metal for methane catalytic combustion, is usually combined with other metals. For instance, Ni is added into the CeO_2 to form binary mixed oxides. The improved catalytic combustion of hydrocarbons is due to the enhanced oxygen storage capacity and redox properties of the catalysts [19,20]. A spectacular activity of the complete conversion below 673 K was recently reported on Ni incorporated cobalt spinel oxides [10]. The monolithically integrated spinel $Ni_{0.5}Co_{0.25}O_4$ nanoarray has also been found having a higher methane oxidation activity than that of Co_3O_4 and $Zn_{0.5}Co_{0.25}O_4$ nanoarrays [4].

Despite widespread investigations and attentions on the complete methane oxidation, a definite reaction mechanism on the transition metal oxide catalysts has yet to be elucidated. The reaction mechanism varies dramatically, depending on the different catalysts and reaction conditions. Debate has been focused on the involvement of dissociative adsorbed oxygen featured suprafacial Langmuir-Hinshelwood (L-H) mechanism, which is often preceded by an Eley-Rideal (E-R) step [6,21], or the lattice oxygen featured intrafacial Mars-van Krevelen (Mv-K) mechanism [6,9,10,22]. Taking the cobalt spinel as an example, some researches have considered the suprafacial reactive oxygen species (ROS), produced from the dissociative adsorption of O_2, as the governing factor that is responsible for the high catalytic activity *via* the L-H mechanism [23,24]. In contrast, the active lattice O and the generated O vacancies implicated in the Mv-K mechanism are regarded to be of vital importance during the catalytic process by other researches [9,22]. The preference or coexistence of the above two mechanistic pathways is actually possible for transition metal oxides with $d^{n>0}$ (for example the spinels and perovskites), due to the metal character of both valence and conduction bands in these oxides [6]. In the early 1980s [25], investigations on the perovskites suggested that not only the adsorbed oxygen but also the lattice oxygen participates in the methane catalytic combustion under different temperatures. This temperature dependent mechanism is also acknowledged over many other mixed metal oxides and spinels [2,4]. Very recently, with the help of both experiment and theoretical studies, Zasada *etc*. offered a more detailed landscape of the interplay between the L-H and Mv-K mechanism over cobalt spinel nanocubes, in which the catalytic process was divided into three temperature windows dominated by different mechanisms [6,22]. From 573 K to 723 K, the L-H mechanism operates, while above 923 K, the Mv-K mechanism dominates. In between, these two mechanisms operate simultaneously. Follow up, their recent work employing the catalytic isotopic investigations and DFT modelling further confirm the operation of both the suprafacial and interfacial mechanisms, which may operate separately and in parallel depending on the reaction temperature and the O_2 pressure. Corresponding Co—O species are proposed to be responsible in the first C—H bond activation which is believed to be the kinetically relevant step. Two three-dimensional enthalpy diagrams have also been provided to discriminate between the above two mechanisms [26]. Aside from the above studies, the routine way to recognize a L-H/E-R or Mv-K pathway is still under study by the reaction rate [6–8]. However, the mechanisms may not be identified properly according to the kinetic data, which exhibit similar rate equations for both L-H/E-R or Mv-K catalytic turnovers [6]. Therefore, simple ways other than kinetic study are in demand to identify and predict the preferential reaction mechanism of certain metal oxide catalyst.

Additionally, in comparison to the well-studied catalytic complete oxidation of methane on palladium or platinum based noble metal catalysts [7,8], the mechanistic studies on spinel oxides are still limited. Recently, Hu *etc*. [10] tried to understand the complete catalytic oxidation of methane on $NiCo_2O_4$ spinel oxides at a molecular level through *in situ* studies and theoretical simulations. Later on, they proposed a complete catalytic cycle of the catalytic combustion of methane over Co_3O_4 [9]. Zasada *etc*. [6,22,26] also provided a molecular understanding of the mechanistic pathways of methane oxidation by both experimental and theoretical studies. Though some inspiring progress have been achieved from these studies, for the complete catalytic oxidation of methane process, it is not yet intrinsically understood at a molecular level of parameters that would trigger the E-R or Mv-K mechanisms. Therefore, further efforts are needed on the exploration of intrinsic origin of the structure-activity/mechanism relations which would provide us with a more comprehensive understanding of the oxidation reaction over transition metal oxides. In particular, there is still lack of pertinent descriptors that are able to capture the physical origin of the activity, which could in turn be used to predict the catalytic behavior of the catalysts.

Using CO oxidation reaction as a probe reaction, our previous studies [27] have provided some fundamental insights into the physiochemical properties of spinel oxides catalysts. These studies interpret the catalytic performance from the view of molecular orbital theory. Nevertheless, compared with the CO oxidation process, the complete catalytic oxidation of methane is far more complicate, during which the CO oxidation is one of the multi-steps [9]. As one of the basic hydrocarbon pollutants with high symmetry, understanding the mechanistic process of methane catalytic oxidation is of vital importance to the complex heterogeneous catalysis and the environmental remediation.

Herein, a series of spinel oxides $ZnNi_xCo_{2-x}O_4$ (x ranging from 0 to 0.8) were synthesized to investigate the origin of the structure-activity/mechanism relationship for complete catalytic oxidation of methane. The catalytic mechanistic process was understood from the perspective of molecular orbital theory by means of experimental results, corroborated by the DFT calculations. In the series $ZnNi_xCo_{2-x}O_4$ spinels, tetrahedral sites were occupied by the inactive Zn^{2+} [22] to ruling out their catalytic contributions, and focus on the catalytically more active octahedral sites [1,28]. Ni was introduced to substitute the octahedrally coordinated Co for a tunable variation in electronic structure. The specific activity normalized by surface area was found to exhibit two different catalytic behaviors under different temperature ranges. It is thereby being proposed that the Ni-poor $ZnNi_xCo_{2-x}O_4$ spinels prefer to follow the suprafacial E-R model, while the Ni-rich $ZnNi_xCo_{2-x}O_4$ spinel catalysts are predominated by the intrafacial Mv-K mechanism. Experiment results are supported by the first principle DFT + U calculations, where the interplay between O *p*-band center and M_{oct} *d*-band center was found to be correlated with not only the methane oxidation activity but also the thermal stability and reaction mechanism of the catalysts. Thermal stable Ni-poor spinel oxides with the M_{oct} *d*-band center in a higher position relative to the O *p*-band center, exhibit greater metal character, indicative of an E-R mechanism. In turn, thermal metastable Ni-rich spinel oxides with the O *p*-band center in a higher position relative to the M_{oct} *d*-band center, display greater oxygen character, indicative of the Mv-K mechanism. The effects of M_{oct} *d*-band center and O *p*-band center were then explained in association with the methane oxidation mechanism. In addition, CH_4-TPD-MS and O_2-TPD tests further confirmed the DFT results with featured involvement of adsorbed oxygen or lattice oxygen. Based above, the relative position between O *p*-band center and M_{oct} *d*-band center was proposed to be activity/mechanism descriptor of the methane complete oxidation on the $ZnNi_xCo_{2-x}O_4$ (x = 0–0.8) spinel oxides.

2. Experimental section

2.1. Synthesis of $ZnNi_xCo_{2-x}O_4$ oxides

$ZnNi_xCo_{2-x}O_4$ spinel oxides were synthesized *via* a thermal decomposition method as described in the supplemental file. Notably, the substitution of Ni for Co, i.e. the value of x in $ZnNi_xCo_{2-x}O_4$ merely varied from x = 0, 0.2, 0.4, 0.6 to x = 0.8. When the Ni replacement reached x = 1, which means equal molar number of $Ni(NO_3)_2{\cdot}6H_2O$ and $Co(NO_3)_2{\cdot}6H_2O$ were added, a mixed phase containing spinel

phases, NiO and ZnO phases started to form. When Co was thoroughly replaced by Ni (x = 2.0), a mixture of NiO and ZnO oxides was formed instead of $ZnNi_2O_4$. Similar situation was reported for the synthesis of $ZnNi_xCo_{2-x}O_4$ nanoparticles [29].

2.2. Materials characterizations

A field emission scanning electron microscope (FESEM) (JEOL JSM-7800 F) was employed for the observation of morphological characteristics of $ZnNi_xCo_{2-x}O_4$ spinel oxides (x = 0–0.8). Their surface areas were obtained *via* Brunauer–Emmett–Teller (BET) analysis and performed by means of an ASAP Tristar II 3020 physisorption analyzer operating at 77 K. The real composition of zinc, nickel and cobalt in the synthesized $ZnNi_xCo_{2-x}O_4$ oxides was determined through an inductively coupled plasma-optical emission spectroscopy (ICP-OES) performed on a Perkin Elmer Avio 200 ICP-OES system. Powder X-ray diffraction (XRD) patterns were collected using Bruker D8 Advance XRD with Cu-K_α radiation (λ = 1.5418 Å). The diffractograms were registered with a scan rate of 2°/min in the 2θ range of 10°–80°. Further structural information was identified by X-ray absorption near edge structure (XANES) and extended X-ray absorption fine structure (EXAFS) characterizations which were carried out at Singapore Synchrotron Light Source, XAFCA beamline [30].

2.3. Catalytic activity measurement and DFT studies

The methane total oxidation catalytic performance was measured in a fixed bed micro reactor with continuous flow under atmospheric pressure. An on-line gas chromatograph with a flame ionization detector (FID) (GC 2060, Sensitive instrumental Co., Ltd., China) was equipped for the inlet and outlet gas stream analysis. Surface area-normalized specific activity was used for the evaluation of catalytic performances of all samples.

The density functional theory (DFT) calculations were performed by the Vienna Ab initio Simulation Package [31], taking advantage of the projected augmented wave (PAW) model. The Perdew-Burke-Ernzerhof (PBE) functional [32] was used to treat the exchange and correlation effect. The GGA + U calculations were performed using the model proposed by Dudarev et al. [33]. Details were given in the supplemental file.

3. Results and discussion

3.1. Materials characterizations

The morphology of $ZnNi_xCo_{2-x}O_4$ oxides (x = 0–0.8) was examined by FESEM. As depicted in Fig. 1a, all samples consist mainly of irregularly shaped particles which are randomly aggregated or stacked into some pore structures. The particle sizes were determined by the N_2 adsorption measurements as presented in Fig. 1b and Table S1. $ZnCo_2O_4$ possess the largest specific surface area of 57 $m^2 g^{-1}$, whereas when Ni was incorporated, the surfaces areas of these Ni-contained samples are gradually decreased from 56 to 38 $m^2 g^{-1}$ (Table S1). Fig. 1c exhibits the XRD patterns of $ZnNi_xCo_{2-x}O_4$ oxides (x = 0–0.8) being synthesized. The diffraction peaks of $ZnCo_2O_4$ (x = 0) can be readily indexed to the standard cubic spinel $ZnCo_2O_4$ (JCPDS Card No. 00-023-1390) without detectable parasitic phases. All the diffraction patterns indicate the retainment of pure cubic spinel structure up to x = 0.8 wherein Co is replaced by Ni. Nevertheless, as the level of substitution of Co by Ni further increases, additional NiO and ZnO phases are formed as shown in Fig. S1. For those pure spinel $ZnNi_xCo_{2-x}O_4$ oxides (x = 0–0.8), an increased lattice parameter (α) is observed from 8.124(7) Å to 8.180(7) Å (Fig. S2 and Table S1) with an increase of Ni substitution. Similar lattice expansion has been reported [34] and can be attributed to the the Jahn-Teller distortion induced by the incorporation of low spin Ni^{3+} ($t_{2g}6\ e_g1$) into the structure [35,36]. The real atomic ratios of Zn:Co:Ni in the series $ZnNi_xCo_{2-x}O_4$ (x = 0–0.8) oxides are confirmed by the ICP-OES as shown in Table S2.

To verify whether Ni and Co remain occupied in octahedral sites as expected when Ni is introduced, EXAFS and XANES measurements were carried out to probe the cation occupancy and valency. Fig. 2a gives the Fourier transform (FT) of the absorption fine structure. Information on site occupation is inferred through revealing bond distances between the absorbing atom and backscattering atoms [37]. Generally, the shell peaks at ~1.5 Å are assigned to single scattering from the closest neighboring crystal oxygen around the absorbing transition metal sites (TM—O bond distance) [37,38]. The peaks at ~2.5 Å (TM_{Oct}-TM_{Oct}) and ~3.0 Å (*e.g.* TM_{Td}-TM_{Td} or TM_{Td}-TM_{Oct}) correspond to scattering of the metal ion to its nearest neighboring metal ion around octahedral or tetrahedral sites [37,38]. That is, octahedrally coordinated cations possess a typical atom-atom bond distance of ~2.5 Å from their neighboring metal ions while tetrahedrally coordinated cations keep the atom-atom bond distances at ~3.0 Å [39]. The FT patterns of both Ni and Co in all the $ZnNi_xCo_{2-x}O_4$ (x = 0–0.8) oxides remain the same with a characteristic interatomic distance of ~2.5 Å, suggesting that all Ni and Co cations are octahedrally coordinated and their coordination environment is not changed by the substitution. This preferential octahedral coordination of Ni and Co cations with a $3d^{6\sim8}$ electron configuration is also supported by the crystal field stability energy [40]. In contrast, the FT EXAFS spectra of Zn with a metal ion-metal ion scattering peak at ~3.0 Å (Zn_{Td}-Zn_{Td}) (Fig. 2a) indicates that Zn is preferentially accommodates at the tetrahedral sites for all the $ZnNi_xCo_{2-x}O_4$ (x = 0–0.8) oxides. The strong preferential tetrahedral site occupancy of divalent Zn in various spinel oxides is attributed to its inactive d^{10} electronic structure [39,41] as reported as well as the large formation energy for antisite defects [42]. Therefore, it can be confirmed that the spinel structure of all the synthesized $ZnNi_xCo_{2-x}O_4$ (x = 0–0.8) oxides is well maintained with Ni, Co cations stays in the octahedral sites and Zn cations fixed in the tetrahedral sites. In addition, the HRTEM image, STEM-EDS image and mapping of $ZnNi_{0.8}Co_{1.2}O_4$ (x = 0.8) provided in the supplementary materials (Figs. S3 and S4) further confirm the phase purity and homogenous distribution of element Zn, Co, Ni and O.

The valency of Co, Ni, Zn in $ZnNi_xCo_{2-x}O_4$ were probed using XANES. The integral method [41,43] was employed to determine the positions of K-edge as shown in Fig. 2b. With the progressive Ni substitution (from x = 0 to x = 0.8), the edge positions of Co, Ni and Zn rarely change and generally keep the same as the pristine $ZnCo_2O_4$ sample, manifesting an unchanged oxidation state of Co, Ni and Zn cations in the $ZnNi_xCo_{2-x}O_4$ when x increases from 0 to 0.8. However, as illustrated in Fig. S5, the K-edge positions of Ni in $ZnNi_xCo_{2-x}O_4$ (x = 1.2, 1.6, 2.0) progressively shift and approach lower binding energies which are closer to that of NiO, suggesting the decrease in oxidation state of Ni cations. Furthermore, a significant increase of peak features at around 9665 eV and a decrease of peak features at around 9675 eV in the Zn K-edge in $ZnNi_{1.2}Co_{0.8}O_4$, $ZnNi_{1.6}Co_{0.4}O_4$ and $ZnNi_2O_4$ (Fig. S5) indicate the appearance of ZnO wurtzite phase [44]. The information presented above further supports the formation of additional NiO and ZnO when the Ni substitution exceeds 0.8 as observed in XRD.

3.2. Catalytic performance evaluation for complete oxidation of methane

A complete oxidation of methane using the as-synthesized $ZnNi_xCo_{2-x}O_4$ spinels (x = 0~0.8) was then performed. For a better reflection of the intrinsic specific activity instead of the mass activity, the methane conversion of these catalysts was normalized to their BET surface areas since catalytic process basically occurs only on the catalyst surface [43,45]. Even though the BET surface area is not perfectly equivalent to the real active surface area, it has been widely used as the best representative for the activity assessment [2,41,46,47]. Typically, the BET surface area has been established as a methodology for activity

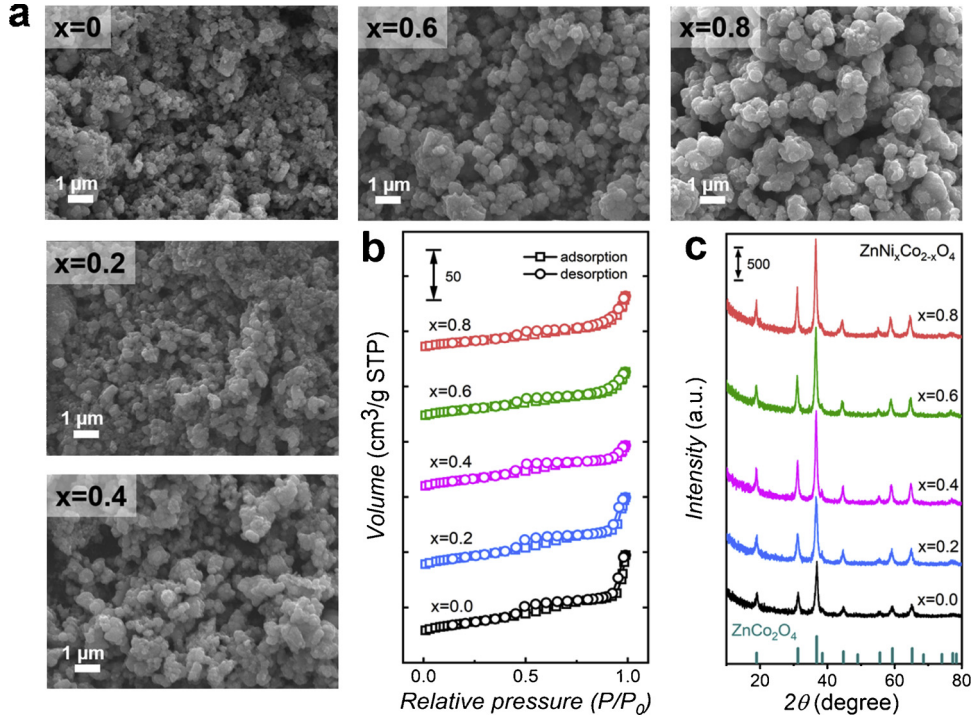

Fig. 1. (a) FESEM images; (b) N_2 adsorption measurements (the detailed data results are given in Table S1) and (c) XRD patterns of the as-prepared $ZnNi_xCo_{2-x}O_4$ (x = 0–0.8) spinel oxides.

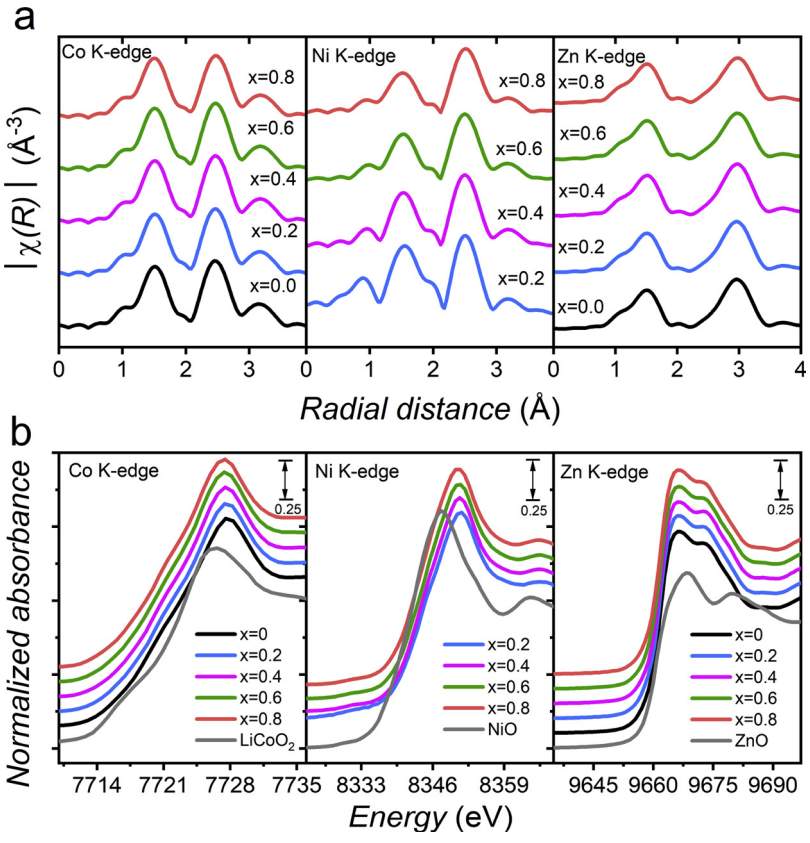

Fig. 2. (a) Fourier transform of EXAFS spectra and (b) Normalized XANES spectra of Co K-edge, Ni K-edge, and Zn K-edge in $ZnNi_xCo_{2-x}O_4$ (x = 0–0.8) spinel oxides.

assessment and screening for metal oxide catalysts [41,46,48]. Fig. 3a shows the surface area normalized specific activity plotted as a function of Ni content in $ZnNi_xCo_{2-x}O_4$ (x = 0–0.8) spinels under various temperatures (from 573 K to 823 K). Generally, the results enable us to distinguish different activity trends depending on the temperatures. Under low temperatures (below 673 K), $ZnNi_{0.2}Co_{1.8}O_4$ (x = 0.2) catalyst exhibits a higher specific activity with a volcano trend than the other four spinels (x = 0, 0.4, 0.6, 0.8). As the temperature increases

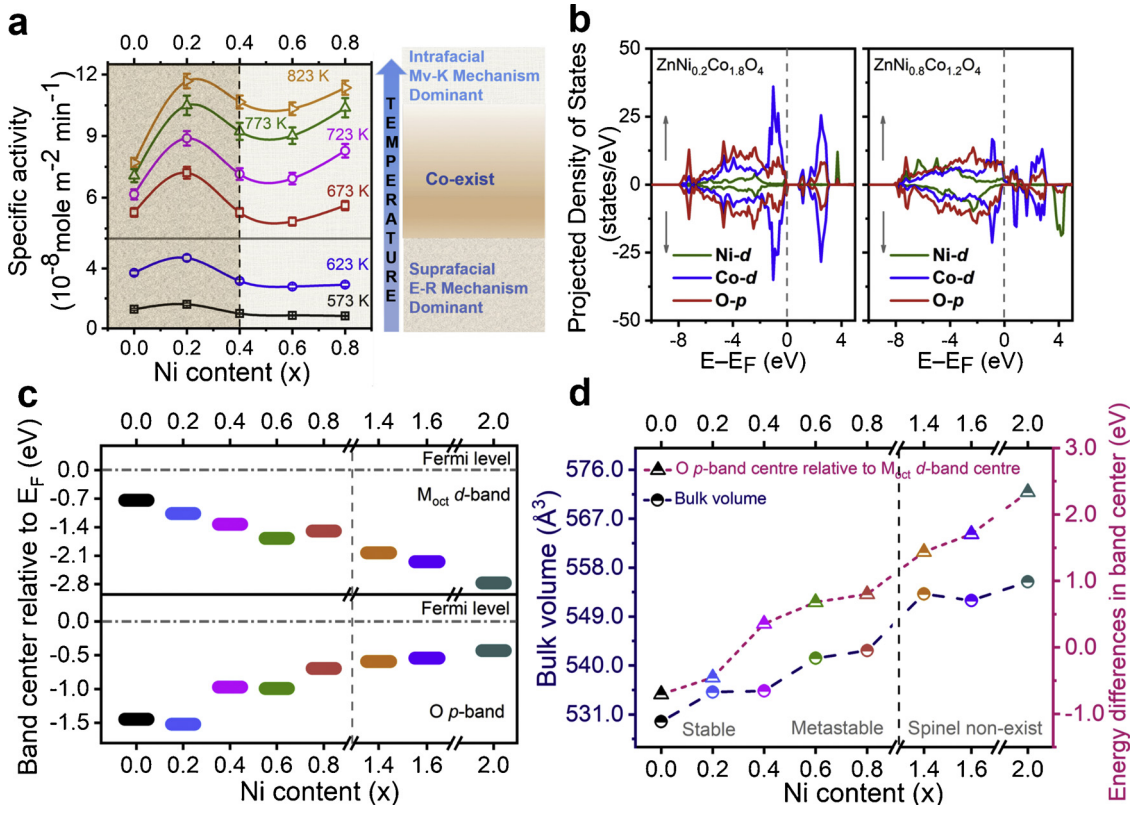

Fig. 3. (a) Normalized specific activities of complete methane oxidation as a function of catalyst compositions for $ZnNi_xCo_{2-x}O_4$ (x = 0–0.8) under increasing temperatures; (b) PDOS of the O *p* states and M_{oct} *d* states in $ZnNi_{0.2}Co_{1.8}O_4$ and $ZnNi_{0.8}Co_{1.2}O_4$, the arrows refer to spin up and spin down projection; (c) Calculated M_{oct} *d*-band center relative to the Fermi level and O *p*-band center relative to the Fermi level of $ZnNi_xCo_{2-x}O_4$ (x = 0–2.0); (d) Calculated bulk volume and O *p*-band center relative to M_{oct} *d*-band center of $ZnNi_xCo_{2-x}O_4$ (x = 0–2.0). Three regions are distinguished with the increased amount of Ni ratio.

(above 673 K), the specific activities are increased for all the catalysts. Under the situation of relatively higher temperatures (673 K–773 K), two distinct catalytic behaviors can be observed. For catalysts with Ni content less than 0.4, the volcano trend remains, indicating the specific activities increase at a similar rate with elevated temperatures. By contrast, for those catalysts with Ni content exceed 0.4, the activities increase more significantly than that of the catalysts with Ni content less than 0.4. It is noteworthy, this activity increment difference becomes more obvious under high temperatures (i.e. 723 K and 773 K). The reaction rate of $ZnNi_{0.8}Co_{1.2}O_4$ (x = 0.8) has achieved 11.7 × 10^{-8} mol m^{-2} min^{-1} at 823 K, keeping pace with the superior activity of $ZnNi_{0.2}Co_{1.8}O_4$ (x = 0.2). Meanwhile, the reaction rates of $ZnNi_{0.6}Co_{1.4}O_4$ and $ZnNi_{0.4}Co_{1.6}O_4$ have increased to a comparable level of 10 × 10^{-8} mol m^{-2} min^{-1}. Notably, the excellent activity of $ZnNi_{0.2}Co_{1.8}O_4$ (x = 0.2) and $ZnNi_{0.8}Co_{1.2}O_4$ (x = 0.8) is comparable, or superior to many of the reported metal oxides catalysts, such as the spinel $M_xCo_{3-x}O_4$ (M = Co, Ni, Zn) [4], $MgCr_2O_4$ and $CoCr_2O_4$ spinels [49], $NiO/Ce_{0.75}Zr_{0.25}O_2$ [50], $LaMO_3$ perovskites [8,14] and so on. It is even approaching to some noble metal catalysts, for instance, the Pt/Al_2O_3 and Pd/Al_2O_3 being reported [7,8]. Kinetic studies including Arrhenius plots of the catalysts for the catalytic methane oxidation and their corresponding activation energies (E_a) are given in Fig. S6 and Table S3.

Generally, two alternate mechanistic pathways are recognized to be involved in the complete oxidation of lean methane, the suprafacial Langmuir-Hinshelwood (L-H) mechanism (involvement of adsorbed oxygen) which is often preceded by an Eley-Rideal (E-R) step [6,51], and the intrafacial Mars-van Krevelen (Mv-K) mechanism (participation of lattice oxygen). Compared with the d^0 transition metal oxides for instance V_2O_5, WO_3, which usually considered to follow the Mv-K mechanism for hydrocarbon oxidation [6,52], the situation is more complicated in the case of spinels or perovskites with $d^{n>0}$. With a metal character for both valence and conduction bands in spinel oxides, the preference or coexistence of the above two mechanistic pathways are possible and is controlled by reaction conditions [6]. Thus, contradictory results have been reported involving intrafacial Mv-K mechanism and suprafacial E-R mechanism for methane oxidation on spinel oxide catalysts [4,8,10,22]. Despite the existence of ambiguities of the mechanistic pathways on various transition metal oxides catalysts, a consensus is met with the temperature dependent reaction kinetic that the L-H/E-R mechanism operates at low temperature range, whilst the Mv-K mechanism features at high temperatures. In between, these two mechanisms engaged simultaneously and may compete with each other [6,9,22,25,51].

Based on the above mechanistic pathways, we hereby proposed that the spinel catalysts presented here may operate in two different mechanisms depending not only on the reaction temperatures but also on the catalysts *per se*. $ZnNi_xCo_{2-x}O_4$ spinels with Ni content less than 0.4 (Ni-poor spinels) prefer to follow the suprafacial E-R model, while $ZnNi_xCo_{2-x}O_4$ spinel catalysts with Ni content exceed 0.4 (Ni-rich spinels) are predominated by the intrafacial Mv-K mechanism. In the temperature range predominated by certain reaction pathways, the activity of those catalysts that follow the same mechanistic pathways gets strengthened; in the converse situation the activity is relatively weakened. Therefore, below 673 K where the suprafacial E-R mechanism operates, the specific activities of Ni-poor spinels are higher than that of the Ni-rich spinels. At the temperature of 673 K–773 K, due to the onset of the intrafacial Mv-K mechanism the specific activities of Ni-rich spinels gradually increased and the activity increment become more significant than that of the Ni-poor spinels. Particularly, when the temperature reaches above 723 K, where the intrafacial Mv-K mechanism gradually dominates the scheme, the activities of Ni-rich spinel

catalysts increase much more. In between, $ZnNi_{0.4}Co_{1.6}O_4$ (x = 0.4) may possess a property that follows both suprafacial and intrafacial mechanisms. This explains why its specific activity increases at a rate comparable to the Ni-rich spinels under high temperature ranges (Mv-K mechanism gradually dominates) but follow the volcano trend of the Ni-poor spinels (coexists of E-R and Mv-K mechanisms).

3.3. DFT studies for origin exploration of structure-performance relationship

Taking into account that catalytic activity is highly related to the catalyst's electronic structure [27,40,53,54], first-principles DFT + U calculations were carried out to testify and interpret the intrinsic structure-performance relationship being proposed. It is well known that the suprafacial E-R mechanism is featured by the dissociative adsorption of dioxygen [16,22,23], while remarkable lattice O activation and oxygen vacancies generation features to the intrafacial Mv-K mechanism [4,6,10]. Therefore, the metal *d*-band center which relates to the adsorption of molecules at metal surface and subsequent adsorbate-metal interactions [55,56], as well as the O *p*-band center which correlated with many oxygen interacting processes, for instance, oxygen dissociation, activation of oxygen, O vacancy hopping, *etc*. [27,54,57], are employed as parameters for the investigation. Furthermore, the interplay between the metal *d*-band center and the O *p*-band center is also examined for the intrinsic catalytic mechanism exploration.

As shown in Fig. 3b, lattice oxygens are observed to be substantially bound to the cations for spinel $ZnNi_{0.2}Co_{1.8}O_4$. In this case, the M−O bond is relatively tighter, indicating a higher possibility to follow the suprafacial E-R mechanism without participation of lattice O. With increased Ni content, non-bonding oxygen *p* states appear on spinel $ZnNi_{0.8}Co_{1.2}O_4$. The appearance of non-bonding oxygen suggests that lattice O is more prone to participate *via* the intrafacial Mv-K reaction pathway. This mechanistic pathway alteration is then further elucidated from the relative position relationship between M_{oct} *d*-band center (relative to E_F) and O *p*-band center (relative to E_F).

The specific values of M_{oct} *d*-band center and O *p*-band center relative to the Fermi level for $ZnNi_xCo_{2-x}O_4$ (x = 0–2.0) are given in Fig. 3c. It can be seen, the position of M_{oct} *d*-band centers gradually move further to the Fermi level with increasing amount of Ni from x = 0 to x = 2.0. For the spinel $ZnNi_xCo_{2-x}O_4$ (x = 0–0.8), the values of M_{oct} *d*-band center decrease from −0.74 eV to −1.68 eV and gets even lower to −2.77 eV for the non-spinel $ZnNi_2O_4$ (x = 2.0). On the contrary, the O *p*-band centers progressively move closer to the Fermi level. The values of O *p*-band centers increase from −1.52 eV to −0.70 eV for the five spinel catalysts, and further increases to −0.43 eV for the non-spinels. To elucidate the interplay of M_{oct} *d*-band center and O *p*-band center, the relative positions between them (the position of O *p*-band center to the Fermi level minus the position of M_{oct} *d*-band center to the Fermi level) have been calculated in Figs. 3d and 4 (schematic display). Realizing that the relative position of O *p*-band and M_{oct} *d*-band level offers a dimension in which both cationic and anionic redox capacities of the catalysts can be cumulated [58], affecting both the reactivity/mechanism and to some extent, the structural thermal stability of the catalysts [59], we therefore compared them with the calculated bulk volume of all the $ZnNi_xCo_{2-x}O_4$ (x = 0–2.0) oxides. For Ni-free $ZnCo_2O_4$ (x = 0), the position of O *p*-band center is 0.71 eV lower than of the position of M_{oct} *d*-band center. This position difference with a lower O *p*-band center is narrowed to 0.46 eV for $ZnNi_{0.2}Co_{1.8}O_4$ (x = 0.2) spinel. When the Ni content increases to x = 0.4, the position of O *p*-band center becomes higher than that of the M_{oct} *d*-band center, and this position difference with a higher O *p*-band center grows larger with the increase Ni content (x > 0.4).

With regarding to the catalysts' thermodynamic stability which associated with the surface structure, it is found to be correlated to the activation of surface oxygen atoms (surface lattice O) [58,59]. For those Ni-poor spinels with a lower energy state of O than that of the M_{oct}, indicating a relatively inactive lattice oxygen and a strong binding of adsorbates to the cations [56]. At this energy state, the surface structure of Ni-poor spinels are thermodynamically stable and their corresponding bulk volume is relatively small. When the Ni content continuously increased to x = 0.4 ($ZnNi_{0.4}Co_{1.6}O_4$), the energy state of O becomes higher than that of M_{oct}, suggesting the trigger of lattice oxygen activation [58,59]. Due to a relatively close energy state of O (−1.0 eV) and M_{oct} (−1.3 eV), the surface structure of $ZnNi_{0.4}Co_{1.6}O_4$ (x = 0.4) is still stable. As the Ni content further increase to x = 0.8, the energy gap between O and M_{oct} gradually increases with a higher O energy state. Under this energy state situation (x = 0.6–0.8), the lattice oxygen gets more active and consequently destabilize the surface [59] of the Ni-rich spinels to a thermodynamically metastable state. Moreover, when the Ni substitution gets too high, to the extent where the energy state of O *p*-band center is much higher than that of the M_{oct} *d*-band center (x > 0.8), drastic structural reorganization might occur [59] and both the surface and bulk structure becomes too unstable to be maintain in a pure-phase spinel structure. This result is in line with the constantly increased bulk volume being calculated (Fig. 3d) and is evidenced by the XRD characterization, where an increased lattice parameter in spinel $ZnNi_xCo_{2-x}O_4$ (x = 0–0.8) is observed as well as the detection of phase separation into wurtzite structure and rock-salt structure with the Ni substitution exceeds 0.8 (x > 0.8).

This relative position relationship between O *p*-band center (relative to E_F) and M_{oct} *d*-band center (relative to E_F) also render the change of mechanistic pathways. As can be seen from the schematic display in Fig. 4, Ni-poor spinels with the M_{oct} *d*-band center in a higher position relative to the O *p*-band center, exhibit greater metal character, indicative of a mechanism centered on the interaction on the metal cation sites [58,60]. Therefore, the L-H/E-R mechanism featured by the adsorption of O_2/CH_4 on the metal surface, dominates the reaction pathway of Ni-poor spinels. In contrast, the Ni-rich spinels with the O *p*-band center in a higher position relative to the M_{oct} *d*-band center, and the Fermi level moves closer to the O *p* states, display greater oxygen character, indicates an enhanced activation of lattice oxygen [60] and a mechanism highlight by the high involvement of lattice oxygen, i.e. the Mv-K mechanism. The interplay between the O *p*-band center and M_{oct} *d*-band center well rationalizes the reactivity of spinel $ZnNi_xCo_{2-x}O_4$ (x = 0–0.8) towards methane conversion and their different mechanistic pathways being predicted previously. This changing of reaction pathways with compositional variation has also been reported for the Ce-doped SnO_2, where the reaction pathway for Sn-rich catalysts follow the Mv-K model, and shift to a more complex model upon the Ce-rich ones [2].

To explicate the reactivity behavior more specifically, the possible E-R and Mv-K pathways for methane oxidation over the Ni-poor and Ni-rich spinel catalysts are proposed in Fig. 4. For Ni-poor spinels that follows the suprafacial E-R mechanism: Step 1, the adsorption of O_2 on the surface of metal oxide (O-M_{oct}-O) and formation of the reactive oxygen species (O_{ads}); Step 2, adsorption and activation of gaseous CH_4 by the adsorbed reactive O, at this step, the surface stabilized $-O_{ads}H$ and $-CH_3$ species are formed; Step 3, with the activation of methane oxidation, some intermediate oxygenates are derived, leading to the subsequent formation of H−O, C−O bonds and the cleavage of residual C−H bonds. Notably, these series intermediates steps, depending on the exact reaction conditions, may create complex networks of consecutive or parallel processes [6]; Step 4, desorption of the produced CO_2 and H_2O for the recovery of active sites on the surface of metal oxides. Among this process, the first C−H cleavage and the H_2O desorption are generally considered to be the rate-determining steps [2,6,16,61] for the methane oxidation. Consequently, when the M_{oct} *d*-band center is too far from the Fermi level (x = 0.4), adsorption of the surface intermediates (reactive O species, *etc*.) on the metal cations is too weak, leading to a lack of stability for the subsequent surface reactions (including the rate-determining step, C−H bond dissociation/activation). In contrast, if the M_{oct} *d*-band center is too close to the Fermi level

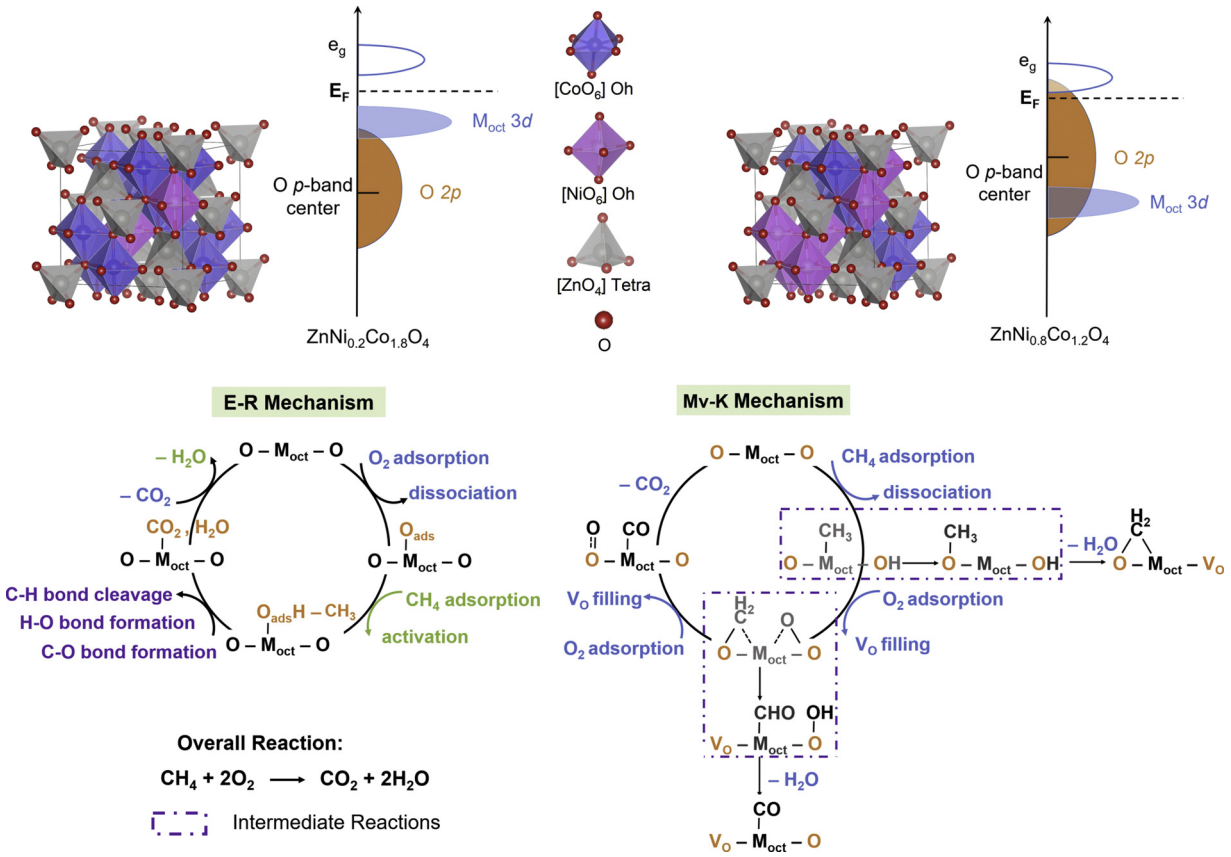

Fig. 4. Spinel structures and schematic representation of the O *p*-band center and M_{oct} *d*-band center for $ZnNi_{0.2}Co_{1.8}O_4$ (top left panel) and $ZnNi_{0.8}Co_{1.2}O_4$ (top right panel); the proposed reaction pathways based on the Eley-Rideal (E-R) mechanism (bottom left panel) for Ni-poor spinel oxides and Mars-van Krevelen (Mv-K) mechanism (bottom right panel) for Ni-rich spinel oxides. M_{oct} refers to cations at the octahedral site, O_{ads} refer as reactive oxygen species and V_o refers to oxygen vacancy. The rate-limiting steps are marked with green; the important adsorbates on the M_{oct} sites in the E-R pathway and the lattice O and generated oxygen vacancies in the Mv-K pathways are marked with orange; the series intermediate reactions are marked with purple (For interpretation of the references to colour in this figure legend, the reader is referred to the web version of this article).

(x = 0), represents the adsorption is too strong, inhibits the desorption (mobility) of formed H_2O (rate-determining step) and thus passivating the active sites. The moderate M_{oct} *d*-band center of $ZnNi_{0.2}Co_{1.8}O_4$ (x = 0.2) optimizes/counterbalances the binding strength of reaction intermediates on surfaces (neither too strong nor too weak), not only facilitates the H_2O transfer but also stabilize the surface intermediates, thus interprets its activity outperformance. Actually, this volcano-type correlation between the catalytic activity and the *d*-band center has widely been reported in the oxygen evolution reaction [59,60,62] and CO oxidation [63] over metal alloy and transition metal oxides. Furthermore, the moderate binding on the surface of $ZnNi_{0.2}Co_{1.8}O_4$ (x = 0.2) is also supported by the temperature programmed desorption of oxygen (O_2-TPD) and temperature programmed desorption of methane coupled with mass spectra (O_2-TPD-MS) tests as depicts in Figs. S8–S10.

Regarding the Ni-rich spinels that follows the intrafacial Mv-K mechanism: Step 1, adsorption and dissociation of gaseous CH_4 on the metal cations (O-M_{oct}-O); Step 2, after dissociation of first C—H in CH_4, the H species will couple with the O atom of the lattice O to form OH, follow by the oxidation of CH_3 species to CH_3O. After that, intermediates CH_2O is formed through dehydrogenation by the OH species and generates the oxygen vacancies; Step 3, molecular oxygen adsorbs and dissociates on the surface O vacancies and fills in; Step 4, H atoms dissociate from the intermediate CH_2O couple with the dissociated intermediate O to form OH and the intermediate CHO is formed by the formation of lattice O vacancy; intermediate CHO is transformed to intermediate CO through dehydrogenation by the formed OH species; Step 5, with further O_2 adsorption and O vacancy refilling, CO is oxidized to CO_2 and be desorbed from the metal cation's surface, leaving the recovered active sites. Among the above processes, the multiple lattice O involved steps instead of one or two rate-determining steps are crucial for the entire methane oxidation, depending mainly on the activity/availability of surface lattice O [3,9,12]. Besides, the well-recognized critical C—H bond cleavage step is also largely controlled by the redox mechanism involving lattice O [61,64]. Therefore, Ni-rich spinels with increased amount of Ni, the O *p*-band center moves closer to the Femi level, the surface lattice O becomes more active and thus facilitates the proceeding of multiple lattice O involving steps, results in the higher specific activity of $ZnNi_{0.8}Co_{1.2}O_4$ (x = 0.8) under high temperature ranges. This enhanced active lattice oxygen participation with increased substitution of Co by Ni in $ZnNi_xCo_{2-x}O_4$ (x = 0–0.8) is also testified by CH_4-TPD-MS and O_2-TPD tests as displayed in Figs. S8–S10. Nevertheless, if the O *p*-band center gets further close to the Femi level (x > 0.8), the surface lattice O gets so active that destabilize the surface and bulk structure and leads to the phase separation as mentioned previously. As a matter of fact, the O *p*-band center relative to the Fermi level is found to be capable of describing O involved reaction energies, activation energies and can be used as descriptors for the O addition and removal related processes [57]. For instance, an increase of OER activity has been reported when the O *p*-band center moves closer to the Fermi level using double perovskites, but further upshifts the O *p*-band center to the Fermi level result in decrease of the oxide stability and no increase in the activity [54]. Similar situation is also observed in our previous study regarding the CO oxidation [27].

At the point of x = 0.4 ($ZnNi_{0.4}Co_{1.6}O_4$), where the position of O *p*-band center (−1.0 eV to E_F) and M_{oct} *d*-band (−1.3 eV to E_F) is quite

close to each other (Fig. 3c and d), possessing a property predominated by both the E-R mechanism and Mv-K mechanism. This well explains the activity behavior of $ZnNi_{0.4}Co_{1.6}O_4$ which follows the volcano trend of Ni-poor spinels under low temperature range but increases at a comparable rate to Ni-rich spinels under higher temperatures. Accordingly, we thereby propose that the position of M_{oct} *d*-band center and O *p*-band center relative to the Fermi level may serve as effective descriptors for the surafacial E-R mechanism and intrafacial Mv-K mechanism, respectively. Future work is necessary to fully understand its suitability to other types of oxides.

4. Conclusion

In summary, through the manipulation of octahedral cation in spinel $ZnNi_xCo_{2-x}O_4$ oxides for complete methane oxidation, it was demonstrated that catalytic behavior alteration can be triggered through the substitution of Co by Ni. By combining the experimental results with DFT theoretical calculations, the origin of this activity and reaction pathway difference can be rationalized by the interplay between O *p*-band center and M_{oct} *d*-band center. Ni-poor $ZnNi_xCo_{2-x}O_4$ spinel oxides with a higher positioned M_{oct} *d*-band center relative to the O *p*-band center, exhibit greater metal character, indicative of a L-H/E-R mechanism centered on the interaction on the metal cation sites. In contrast, Ni-rich $ZnNi_xCo_{2-x}O_4$ spinel oxides with the O *p*-band center in a higher position relative to the M_{oct} *d*-band center and the Fermi level moves closer to the O *p* states, display greater oxygen character; this suggests a Mv-K mechanism highlight by the enhanced involvement of lattice oxygen. In the temperature range predominated by certain reaction pathways, the activity of those catalysts that follow the same mechanistic pathways gets strengthened; in the converse situation the activity is relatively weakened. Accordingly, it is proposed that the relative position between O *p*-band center and M_{oct} *d*-band center, captures the physical origin of methane oxidation activity, and can serve as pertinent descriptor of the methane oxidation activity for the $ZnNi_xCo_{2-x}O_4$ (x = 0˜0.8) spinel oxides. It also helps to predict the preferential reaction pathways, providing a strategy to rationalize and tailor highly active transition metal oxide catalysts for complete methane catalytic oxidation and other oxidation reactions.

Acknowledgements

This work was supported by the Singapore Ministry of Education [Tier 1, Grant number RG3/18(S); Tier 2, Grant number MOE2018-T2-2-027], and the Singapore National Research Foundation under its Campus for Research Excellence And Technological Enterprise (CREATE) program SinBeRISE. The authors also acknowledged the support from the Environmental Chemistry and Materials Centre (ECMC) under Nanyang Environment and Water Research Institute (NEWRI), as well as the Sustainable Earth division of the Nanyang Technological University's Interdisciplinary Graduate School (IGS). This research was also supported by the Facility for Analysis, Characterization, Testing and Simulation (FACTS) in Nanyang Technological University for materials characterizations. Nanjing Tech group also appreciates the financial support from the Nanjing Tech University Research Start-up Fund [grant number 38274017111].

Appendix A. Supplementary data

Supplementary material related to this article can be found, in the online version, at doi:https://doi.org/10.1016/j.apcatb.2019.117844.

Supplementary material related to this article can be found, in the online version, and includes some supplementary experimental procedures, kinetic studies, characterization data including the XRD patterns of $ZnNi_xCo_{2-x}O_4$ (x = 0.2, 1.2, 2.0) oxides, XANES spectra of $ZnNi_xCo_{2-x}O_4$ (x > 0.8) oxides, CH_4-TPD-MS and O_2-TPD profiles, BET values, TEM/EDX mapping of $ZnNi_{0.8}Co_{1.2}O_4$ (x = 0.8), ICP results and refined XRD data of $ZnNi_xCo_{2-x}O_4$ (x = 0–0.8) spinel oxides, PDOS of the O *p* states and M_{oct} *d* states for $ZnNi_xCo_{2-x}O_4$ (x = 0, 0.4, 0.6) spinel oxides.

References

[1] J. Li, X. Liang, S. Xu, J. Hao, Appl. Catal. B Environ. 90 (2009) 307–312.
[2] C. Liu, H. Xian, Z. Jiang, L. Wang, J. Zhang, L. Zheng, Y. Tan, X. Li, Appl. Catal. B Environ. 176–177 (2015) 542–552.
[3] V.R. Choudhary, B.S. Uphade, S.G. Pataskar, Appl. Catal. A Gen. 227 (2002) 29–41.
[4] Z. Ren, V. Botu, S. Wang, Y. Meng, W. Song, Y. Guo, R. Ramprasad, S.L. Suib, P.X. Gao, Angew. Chem. Int. Ed. 53 (2014) 7223–7227.
[5] R.J. Farrauto, Science 337 (2012) 659–660.
[6] F. Zasada, J. Janas, W. Piskorz, M. Gorczyńska, Z. Sojka, ACS Catal. 7 (2017) 2853–2867.
[7] P. Gélin, M. Primet, Appl. Catal. B Environ. 39 (2002) 1–37.
[8] T.V. Choudhary, S. Banerjee, V.R. Choudhary, Appl. Catal. A Gen. 234 (2002) 1–23.
[9] W. Hu, J. Lan, Y. Guo, X.M. Cao, P. Hu, ACS Catal. 6 (2016) 5508–5519.
[10] F.F. Tao, J. Shan, L. Nguyen, Z. Wang, S. Zhang, L. Zhang, Z. Wu, W. Huang, S. Zeng, P. Hu, Nat. Commun. 6 (2015) 7798.
[11] J. Chen, X. Zhang, H. Arandiyan, Y. Peng, H. Chang, J. Li, Catal. Today 201 (2013) 12–18.
[12] N. Bahlawane, Appl. Catal. B Environ. 67 (2006) 168–176.
[13] P. Ciambelli, S. Cimino, L. Lisi, M. Faticanti, G. Minelli, I. Pettiti, P. Porta, Appl. Catal. B Environ. 33 (2001) 193–203.
[14] S. Petrović, A. Terlecki-Baričević, L. Karanović, P. Kirilov-Stefanov, M. Zdujić, V. Dondur, D. Paneva, I. Mitov, V. Rakić, Appl. Catal. B Environ. 79 (2008) 186–198.
[15] L. Marchetti, L. Forni, Appl. Catal. B Environ. 15 (1998) 179–187.
[16] S. Pengpanich, V. Meeyoo, T. Rirksomboon, K. Bunyakiat, Appl. Catal. A Gen. 234 (2002) 221–233.
[17] A. Shulman, E. Cleverstam, T. Mattisson, A. Lyngfel, Energy Fuel. 23 (2009) 5269–5275.
[18] L. Hu, Q. Peng, Y. Li, J. Am. Chem. Soc. 130 (2008) 16136–16137.
[19] N. Yisup, Y. Cao, W.L. Feng, W.L. Dai, K.N. Fan, Catal. Lett. 99 (2005) 207–213.
[20] W. Shan, M. Luo, P. Ying, W. Shen, C. Li, Appl. Catal. A Gen. 246 (2003) 1–9.
[21] A. Bielański, J. Haber, Catal. Rev. Sci. Eng. 19 (1979) 1–41.
[22] F. Zasada, W. Piskorz, J. Janas, J. Gryboš, P. Indyka, Z. Sojka, ACS Catal. 5 (2015) 6879–6892.
[23] V.D. Sokolovskii, Catal. Rev. 32 (1990) 1–49.
[24] Y. Takita, T. Tashiro, Y. Saito, F. Hori, J. Catal. 97 (1986) 25–35.
[25] H. Arai, T. Yamada, K. Eguchi, T. Seiyama, Appl. Catal. 26 (1986) 265–276.
[26] F. Zasada, J. Gryboś, C. Hudy, J. Janas, Z. Sojka, Catal. Today (2019), https://doi.org/10.1016/j.cattod.2019.03.061.
[27] T. Wang, Y. Sun, Y. Zhou, S. Sun, X. Hu, Y. Dai, S. Xi, Y. Du, Y. Yang, Z.J. Xu, ACS Catal. 8 (2018) 8568–8577.
[28] J.P. Jacobs, A. Maltha, J.G.H. Reintjes, J. Drimal, V. Ponec, H.H. Brongersma, J. Catal. 147 (1994) 294–300.
[29] J. Kumar, C.R. Mariappan, V. Kumar, S. Murugavel, G.V. Prakash, Mater. Res. Bull. 83 (2016) 632–639.
[30] Y. Du, Y. Zhu, S. Xi, P. Yang, H.O. Moser, M.B.H. Breese, A. Borgna, J. Synchrotron Radiat. 22 (2015) 839–843.
[31] G. Kresse, J. Furthmüller, Phys. Rev. B 54 (1996) 11169–11186.
[32] J.P. Perdew, K. Burke, M. Ernzerhof, Phys. Rev. Lett. 77 (1996) 3865–3868.
[33] S.L. Dudarev, G.A. Botton, S.Y. Savrasov, C.J. Humphreys, A.P. Sutton, Phys. Rev. B 57 (1998) 1505–1509.
[34] S. Hull, J. Trawczyński, Int. J. Hydrogen Energy 39 (2014) 4259–4265.
[35] M.N. Sanz-Ortiz, F. Rodríguez, J. Rodríguez, G. Demazeau, J. Phys. Condens. Matter 23 (2011) 415501.
[36] M. Stoica, C.S. Lo, New J. Phys. 16 (2014) 055011.
[37] C.M.B. Henderson, J.M. Charnock, D.A. Plant, J. Phys. Condens. Matter 19 (2007) 488–490.
[38] H.Y. Wang, S.F. Hung, H.Y. Chen, T.S. Chan, H.M. Chen, B. Liu, J. Am. Chem. Soc. 138 (2016) 36–39.
[39] S. Calvin, E.E. Carpenter, B. Ravel, V.G. Harris, S.A. Morrison, Phys. Rev. B 66 (2002) 224405.
[40] X. Shi, S.L. Bernasek, A. Selloni, J. Phys. Chem. C 120 (2016) 14892–14898.
[41] C. Wei, Z. Feng, G.G. Scherer, J. Barber, Y. Shao-Horn, Z.J. Xu, Adv. Mater. 29 (2017) 1606800.
[42] M.N. Amini, H. Dixit, R. Saniz, D. Lamoen, B. Partoens, Phys. Chem. Chem. Phys. 16 (2014) 2588.
[43] Y. Zhou, S. Sun, S. Xi, Y. Duan, T. Sritharan, Y. Du, Z.J. Xu, Adv. Mater. 30 (2018) 1705407.
[44] B. Henne, V. Ney, K. Ollefs, F. Wilhelm, A. Rogalev, A. Ney, Sci. Rep. 5 (2015) 16863.
[45] Z. Feng, W.T. Hong, D.D. Fong, Y. Lee, Y. Yacoby, D. Morgan, Y. Shao-Horn, Acc. Chem. Res. 49 (2016) 966–973.
[46] T.R. Baldwin, R. Burch, Appl. Catal. 66 (1990) 337–358.
[47] T.R. Baldwin, R. Burch, Catal. Lett. 6 (1990) 131–138.
[48] J. Suntivich, H.A. Gasteiger, N. Yabuuchi, Y. Shao-Horn, J. Electrochem. Soc. 157 (2010) 1263–1268.
[49] J. Hu, W. Zhao, R. Hu, G. Chang, C. Li, L. Wang, Mater. Res. Bull. 57 (2014) 268–273.
[50] S. Thaicharoensutcharittham, V. Meeyoo, B. Kitiyanan, P. Rangsunvigit, T. Rirksomboon, Catal. Commun. 10 (2009) 673–677.

[51] S. Royer, D. Duprez, ChemCatChem 3 (2011) 24–65.
[52] B. Grzybowska-Swierkosz, Top. Catal. 11/12 (2000) 23–42.
[53] F. Calle-Vallejo, O.A. Díaz-Morales, M.J. Kolb, M.T.M. Koper, ACS Catal. 5 (2015) 869–873.
[54] A. Grimaud, K.J. May, C.E. Carlton, Y.L. Lee, M. Risch, W.T. Hong, J. Zhou, Y. Shao-Horn, Nat. Commun. 4 (2013) 2439.
[55] B. Hammer, J.K. Nørskov, Adv. Catal. 144 (2000) 71–129.
[56] B. Hammer, J.K. Norskov, Nature 376 (1995) 238–240.
[57] Y.L. Lee, J. Kleis, J. Rossmeisl, Y. Shao-Horn, D. Morgan, Energy Environ. Sci. 4 (2011) 3966.
[58] A. Grimaud, W.T. Hong, Y. Shao-Horn, J.M. Tarascon, Nat. Mater. 15 (2016) 121–126.
[59] A. Grimaud, A. Demortière, M. Saubanère, W. Dachraoui, M. Duchamp, M.L. Doublet, J.M. Tarascon, Nat. Energy 2 (2017) 16189.
[60] A. Grimaud, O. Diaz-Morales, B. Han, W.T. Hong, Y.L. Lee, L. Giordano, K.A. Stoerzinger, M.T.M. Koper, Y. Shao-Horn, Nat. Chem. 9 (2017) 457–465.
[61] R. Burch, D.J. Crittle, M.J. Hayes, Catal. Today 47 (1999) 229–234.
[62] I.C. Man, H.Y. Su, F. Calle-Vallejo, H.A. Hansen, J.I. Martínez, N.G. Inoglu, J. Kitchin, T.F. Jaramillo, J.K. Nørskov, J. Rossmeisl, ChemCatChem 3 (2011) 1159–1165.
[63] H. Abe, H. Yoshikawa, N. Umezawa, Y. Xu, G. Saravanan, G.V. Ramesh, T. Tanabe, R. Kodiyath, S. Ueda, N. Sekido, Y. Yamabe-Mitarai, M. Shimoda, T. Ohno, F. Matsumoto, T. Komatsu, Phys. Chem. Chem. Phys. 17 (2015) 4879–4887.
[64] D. Ciuparu, E. Altman, L. Pfefferle, J. Catal. 203 (2001) 64–74.

Update

Applied Catalysis B: Environmental

Volume 269, Issue , 15 July 2020, Page

DOI: https://doi.org/10.1016/j.apcatb.2019.118340

Applied Catalysis B: Environmental 269 (2020) 118340

Contents lists available at ScienceDirect

Applied Catalysis B: Environmental

journal homepage: www.elsevier.com/locate/apcatb

Corrigendum

Corrigendum to "Origin of electronic structure dependent activity of spinel $ZnNi_xCo_{2-x}O_4$ oxides for complete methane oxidation" [Appl. Catal. B: Environ. 256 (2019) 117844]

Ting Wang[a,b,c,1], Jieyu Wang[a,1], Yuanmiao Sun[b], Yan Duan[b,d], Shengnan Sun[b,d], Xiao Hu[b,c], Shibo Xi[e], Yonghua Du[e], Chuan Wang[a,*], Zhichuan J. Xu[b,d,**]

[a] Institute of Advanced Synthesis, School of Chemistry and Molecular Engineering, Jiangsu National Synergetic Innovation Center for Advanced Materials, Nanjing Tech University, 30 Puzhu South Road, Nanjing 211800, PR China
[b] School of Materials Science and Engineering, Nanyang Technological University, 50 Nanyang Avenue, 639798, Singapore
[c] Nanyang Environment and Water Research Institute (NEWRI), Interdisciplinary Graduate School (IGS), Nanyang Technological University, 1 Cleantech Loop, CleanTech One, 637141, Singapore
[d] Solar Fuels Laboratory, Nanyang Technological University, 50 Nanyang Avenue, 639798, Singapore
[e] Institute of Chemical and Engineering Sciences A*STAR, 1 Pesek Road, 627833, Singapore

The authors regret "T. Wang and J. Wang contributed equally to this work." was missing in the author contribution information, which is only found in the supporting information.

The authors would like to apologise for any inconvenience caused.

DOI of original article: https://doi.org/10.1016/j.apcatb.2019.117844

* Corresponding author at: School of Materials Science and Engineering, Nanyang Technological University, 50 Nanyang Avenue, 639798, Singapore.
** Corresponding author at: Institute of Advanced Synthesis, School of Chemistry and Molecular Engineering, Jiangsu National Synergetic Innovation Center for Advanced Materials, Nanjing Tech University, 30 Puzhu South Road, Nanjing 211800, PR China.
E-mail addresses: ias_cwang@njtech.edu.cn (C. Wang), xuzc@ntu.edu.sg (Z.J. Xu).
[1] These authors contributed equally to this work.

https://doi.org/10.1016/j.apcatb.2019.118340

Available online 28 February 2020